Petroleum Science 23 (2026) 1089–1104

Contents lists available at ScienceDirect

Petroleum Science

journal homepage: www.keaipublishing.com/en/journals/petroleum-science

Original Paper

Micro-nanoscale pore structure characteristics and enrichment mechanisms of shale oil in mixed sedimentary reservoirs of the Jimusar Sag, Junggar Basin, northwestern China

Lei Xiao [a], Yi-Wen Ju [a,*], Jun Jin [b], Jin Liu [b], Jing-Qiang Tan [c], Shu Jiang [d], Xin Li [e], Bing Hou [f], Peng Qiao [a], Xin-Gao Hou [a], Jian Gao [a]

[a] State Key Laboratory of Earth System Numerical Modeling and Application, College of Earth and Planetary Sciences, University of Chinese Academy of Sciences, Beijing, 101408, China
[b] Research Institute of Experiment and Detection, Xinjiang Oilfield Company, PetroChina, Karamay, 834000, Xinjiang, China
[c] Key Laboratory of Metallogenic Prediction of Nonferrous Metals and Geological Environment Monitoring, Ministry of Education, School of Geosciences and Info-Physics, Central South University, Changsha, 410083, Hunan, China
[d] Key Laboratory of Tectonics and Petroleum Resources, China University of Geosciences, Wuhan, 430074, Hubei, China
[e] Xinjiang Key Laboratory for Geodynamic Processes and Metallogenic Prognosis of the Central Asian Orogenic Belt, Xinjiang University, Urumqi, 830047, Xinjiang, China
[f] School of Petroleum, China University of Petroleum-Beijing at Karamay, Karamay, 834000, Xinjiang, China

ARTICLE INFO

Article history:
Received 21 February 2025
Received in revised form
31 July 2025
Accepted 14 October 2025
Available online 24 October 2025

Edited by Xi Zhang and Jie Hao

Keywords:
Jimusar Sag
Shale oil
Occurrence state
Pore structure
Fractal dimension

ABSTRACT

The successful development of shale oil in the United States has completely changed the global energy landscape. In recent years, shale oil in the Junggar Basin in China has attracted widespread attention. The Permian Lucaogou Formation in the Junggar Basin features a mixed sedimentary reservoir with a complex pore structure, which hinders the understanding of the micro- and nano-scale enrichment process of shale oil. In this paper, high-pressure mercury injection (HPMI), low-temperature nitrogen adsorption (LTNA), and laser scanning confocal microscopy (LSCM) are conducted to quantitatively characterize the pore structure of the reservoir. The results show that the pore size distribution is bimodal, with the main peak appearing near 1.89–3.15 nm and the secondary peak appearing near 30.75–84.58 nm. The specific surface area (SSA) ranges from 3.155 m^2/g to 20.681 m^2/g, and the mesopores are the main contributor. The pore space is characterized by multiple fractals, with D_M ranging from 2.0366 to 2.9872 derived from high-pressure mercury injection. The D_{N1} and D_{N2} obtained from low-temperature nitrogen adsorption are 2.1662–2.6254 and 2.0768–2.7283. Oil content is strongly influenced by reservoir porosity. The fractal characteristics of pores (2.32–36.90 nm) have a more obvious effect on oil content. The maturity stage of organic matter determines the generation of light and heavy components in shale oil, while the coupling of charging force and pore capillary resistance controls the enrichment pattern of light components in the pore center and heavy components in the pore edge. The results are helpful for the optimization of favorable shale oil blocks and provide theoretical guidance for the exploration of oil and gas resources and the development of oil recovery technology.

1. Introduction

Recent rapid growth in shale oil production in the United States has reshaped the global energy landscape, driving significant transformations in the world oil market (Hopkins, 2017; Wang et al., 2018). The successful development of shale oil in the United States, coupled with advancements in petroleum geology

* Corresponding author.
E-mail address: juyw03@163.com (Y.-W. Ju).
Peer review under the responsibility of China University of Petroleum (Beijing).

https://doi.org/10.1016/j.petsci.2025.10.014

and exploration technologies, has significantly increased the role of unconventional oil and gas reservoirs in exploration and production (Jarvie, 2014). This progress has enabled the United States to achieve energy independence and become the largest oil producer in history, with production expected to continue rising in the future (Mcmahon et al., 2024). Amid the growing challenges in conventional oil and gas exploration, shale oil resources have increasingly become a central focus in contemporary oil exploration and development. With abundant shale oil resources and considerable development potential, China is poised to make a substantial contribution to the global shale oil industry, as its production exceeded 4 million tons in 2023 (Qian et al., 2024). Shale oil resources in China are primarily distributed across the Songliao, Ordos, Junggar, and Bohai Bay basins, among others (Zhao et al., 2019; Wang et al., 2022a; Wu et al., 2022; Zhang et al., 2024). Jimusar in the Junggar Basin, designated as China's first national shale oil pilot zone, contains an estimated 1 billion tons of oil resources (Kuang et al., 2012; Jiang et al., 2015; Zha et al., 2021).

In the exploration and development of shale oil, the occurrence state of oil is related to whether it is movable and recoverable (Liu et al., 2023). The pore structure of the reservoir is an important factor affecting the occurrence state of shale oil and serving as essential parameters for assessing the resource potential of shale oil (Adeyilola et al., 2022). Permian Lucaogou Formation developed a mixed sedimentary reservoir, which is the main shale oil exploration and development of Jimusar Sag, Junggar Basin (Yang et al., 2023). Mixed sediments are formed by the mixed deposition of terrigenous debris and carbonate minerals, and can be found in the marine-continental transition zone, continental shelves and slopes, and continental lakes (García-Hidalgo et al., 2007). Different from conventional single reservoirs, mixed sediments fundamentally affect the characteristics and evolution of reservoirs (Wang et al., 2019).

Previous studies have carried out extensive research on the pore structure characteristics and oil enrichment mechanism of mixed sedimentary reservoirs (Su et al., 2018; Liu et al., 2019; Zhi et al., 2021; Wang et al., 2022b). Palermo et al. (2008) studied the Lower Triassic Rogenstein member of the Buntsandstein Formation and found that the reservoir was controlled by periodic changes in sedimentary facies and relative lake level. Lü et al. (2017) found that the Paleogene Shahejie Formation mixed sedimentary reservoir in the Bohai Bay Basin developed residual primary intergranular pores, paleo-intragranular pores, and feldspar dissolved pores. The formation of early microfacies and pore-lining dolomite played a key role in the preservation of porosity and reservoir oil richness. Li et al. (2021) believed that mineral composition, sedimentary structure and organic matter content affect the development of pore network and storage of shale oil in the Qiketai Formation mixed reservoir in the Tuha Basin. Li et al. (2020) found that the distribution of movable light oil in mixed rock reservoirs is closely related to permeability and the proportion of large intergranular pores, while the distribution of immobile heavy oil and water in nanopores is affected by factors such as small pores, solid organic matter and clay minerals. Pan et al. (2021) studied the Permian Lucaogou Formation mixed reservoir in the Santanghu Basin and found that tuffaceous materials made the pore structure more complex. Körmös et al. (2023) studied the Eocene mixed clastic-carbonate rock sequence in the Paleogene Basin of Hungary and found that the early diagenetic process increased the porosity, while the transformation and cementation of kaolinite in the late diagenetic process led to a decrease in porosity, which in turn affected the development of reservoir micro-nanostructure and shale oil enrichment mechanism. Zhang et al. (2023b) found that the lacustrine mixed reservoir of the Ganchaigou Formation in the Qaidam Basin has multi-fractal characteristics, and the heterogeneity of the pore structure is correlated with porosity, permeability and oil and gas development potential. However, the micro-nano storage capacity of shale oil in mixed rock reservoirs has not been fully understood, and the microscopic occurrence state and enrichment mechanism of shale oil are still unclear.

Although previous studies have explored the pore structure of mixed sedimentary reservoirs and the influencing factors of shale oil occurrence, few have systematically combined multiple technical means to directly and indirectly quantitatively characterize the multi-scale pore system and the microscopic oil occurrence state. This study uniquely integrates indirect methods such as high-pressure mercury injection (HPMI), and low-temperature nitrogen adsorption (LTNA) with direct observation such as laser scanning confocal microscopy (LSCM), and introduced fractal theory to comprehensively characterize the pore structure of the shale oil reservoir in the Jimusar Sag, Junggar Basin. By analyzing the pore structure and oil content of different types of mixed sedimentary reservoirs, the controlling effect of pore structure on the distribution of shale oil is studied, and the micro-nano scale occurrence state of shale oil in mixed sediments is identified, providing new insights into the microscopic enrichment mechanism of shale oil in mixed rock reservoirs. The results are of scientific significance to the establishment of shale oil enrichment theory of mixed sedimentary reservoirs, and also provide guidance for the exploration of shale oil resources and the development of oil recovery technology.

2. Geological background

The Junggar Basin is located in the southern part of the paleo-Asiatic tectonic domain, which has developed into the multi-cycle superimposed petroleum basin (Ju et al., 2022; Fig. 1(a)). The primary structural units within the basin are categorized into six distinct regions: the Ulungu Sag, the Luliang Uplift, the Western Uplift, the Central Sag, the North Tianshan Piedmont Thrust Belt, and the Eastern Uplift (Fig. 1(b)). The Jimusar Sag, situated within the Eastern Uplift, has garnered significant attention in recent years due to advancements in tight oil development within the Permian Lucaogou Formation (Qu et al., 2017; Yang et al., 2018, 2019; Lin et al., 2021; Zhang et al., 2022).

The Jimusar Sag is delineated to the north by the Jimusar Fault, to the south it connects with the Fukang Fault Zone via the Santai and Xidi Faults, to the west it is linked to the Beisantai Uplift by the Xidi and Laozhuangwan Faults, and to the east, it is bordered by the Xidi and Laozhuangwan Faults connecting again with the Beisantai Uplift (Fig. 1(c); Hou et al., 2021; Liu et al., 2021). The ancient Western Uplift, in contrast, is generally characterized as a basket-shaped sag, with a shallower western region and a deeper eastern section, underlain by the Carboniferous fold basement (Fig. 1(d)).

Since the Carboniferous period, the Jimusar Sag has experienced multiple tectonic phases, notably the Hercynian, Indosinian, Yanshan, and Himalayan orogenies. Sediments from the Carboniferous, Permian, Triassic, Jurassic, Cretaceous, Eocene, Neogene, and Quaternary periods were sequentially deposited. The Lucaogou Formation in the Permian, deposited in the semi-deep to deep lacustrine facies and widely distributed throughout the sag, is an important hydrocarbon-generating layer and shale oil occurrence interval in the study area (Pang et al., 2022; Liu et al., 2024).

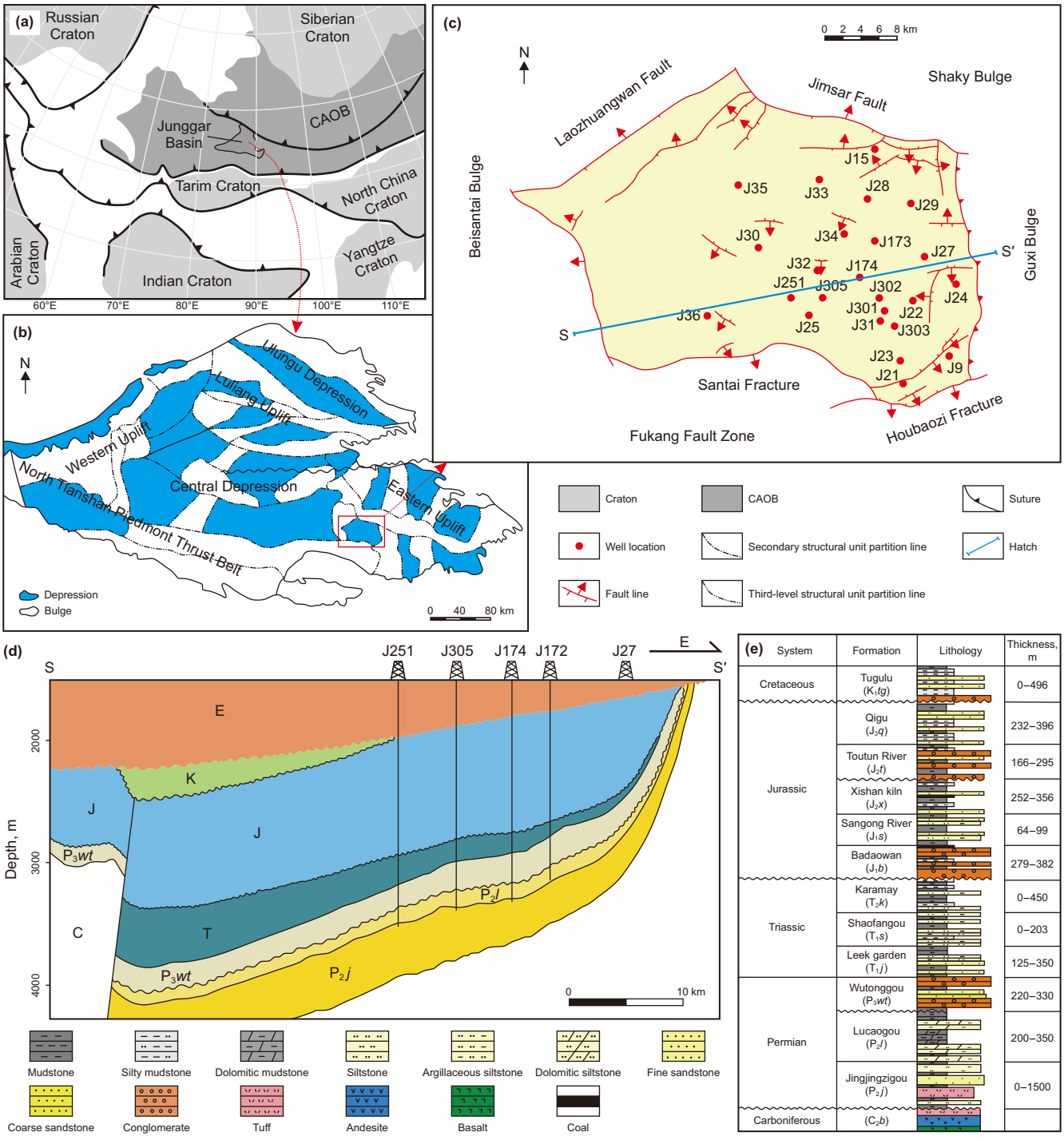

Fig. 1. Geological setting of Jimusar Sag in Junggar Basin (modified from Qu et al., 2019). (**a**) Tectonic location of the Junggar Basin. (**b**) Location of Jimusar Sag in Junggar Basin. (**c**) Structural map of the Jimusar Sag. (**d**) General stratigraphy of cross section SS'. (**e**) Stratigraphic column of the Jimusar Sag.

3. Sampling and methods

3.1. Sample collection

A total of thirty-two core samples were collected from nine shale oil wells located in the "sweet spot" interval of the Lucaogou Formation within the Jimusar Depression of the Junggar Basin. These samples, representative of the shale oil reservoir, were selected to cover a range of lithologies and organic matter contents. These samples were subsequently analyzed using various techniques, including overburden porosity measurement, HPMI, LTNA, and LSCM.

3.2. Laser scanning confocal microscopy

After slicing, the oil-bearing samples were immediately frozen in liquid nitrogen and air-dried at 5 °C. To prepare the samples for observation, they were ground to a thickness of 0.04–0.05 mm. The

samples were then examined using a LEICA SP5II laser scanning confocal microscope at 25 °C, with a relative humidity range of 30%–46% (Fig. 2(a)). Excitation was achieved using a fixed-wavelength laser set at 488 nm. Fluorescence signals from the light components of the crude oil were detected in the 490–600 nm range, while the heavier components emitted signals within the 600–800 nm range. A total of 7–10 image scans were performed, and the scanned images were processed and reconstructed in three dimensions using Imaris 7.2 software.

3.3. Overburden porosity

The porosity and permeability of the mixed sediments cores were measured following the GB/T 29172-2012 Core Analysis Method to ensure consistency with industry standards. An NDP-605 ultra-low permeability meter was employed to determine gas permeability, while a helium porosity meter was used to measure porosity (Fig. 2(b)). The helium porosity measurements were conducted under overburden pressure conditions to account for in-situ stress effects, thereby providing more accurate reservoir property estimates.

3.4. High-pressure mercury injection

The HPMI method utilizes the AutoPore 9510-IV instrument to inject mercury into a core sample measuring 2.5 cm in diameter and 2.5 cm in height (Fig. 2(c)). Prior to mercury injection, the samples were dried in a vacuum oven at 60 °C for 24 h to remove residual moisture. To prevent pore deformation under high pressure, the maximum pressure during the injection process is restricted to 200 MPa. The pore throat test range is between 3 nm and 800 μm. Following Washburn and Fooyitt (1921), the distribution characteristics of the pore throat sizes can be determined.

3.5. Low-temperature nitrogen adsorption

The LTNA experiment was performed using an ASAP 2460 fully automated surface area and porosity analyzer to characterize the pore structure and surface area of the samples (Fig. 2(d)). A 3 g sample was finely ground to a particle size of less than 250 μm before being loaded into a sample tube, and its initial weight was recorded. The sample tube was then sealed and placed in a degassing station, where a heating jacket was applied to maintain a controlled temperature during the degassing process. The vacuum pump was activated to remove any adsorbed gases from the sample surface. Upon completion of degassing, the sample was re-weighed to ensure complete gas removal, and the final weight was recorded. Subsequently, the sample tube was immersed in liquid nitrogen, and nitrogen adsorption measurements were conducted at various relative pressures using the ASAP 2460 analyzer. The resulting adsorption isotherms were used to evaluate the specific surface area (SSA), pore size distribution, and total pore volume (TPV) of the shale oil reservoir samples.

3.6. Calculation of pore fractal dimension

Fractal theory is commonly applied to characterize the heterogeneity and complexity of pore structures (Mandelbrot, 1967; Bu et al., 2015; Li et al., 2017). The fractal dimension typically ranges from 2 to 3 and is often determined using techniques like

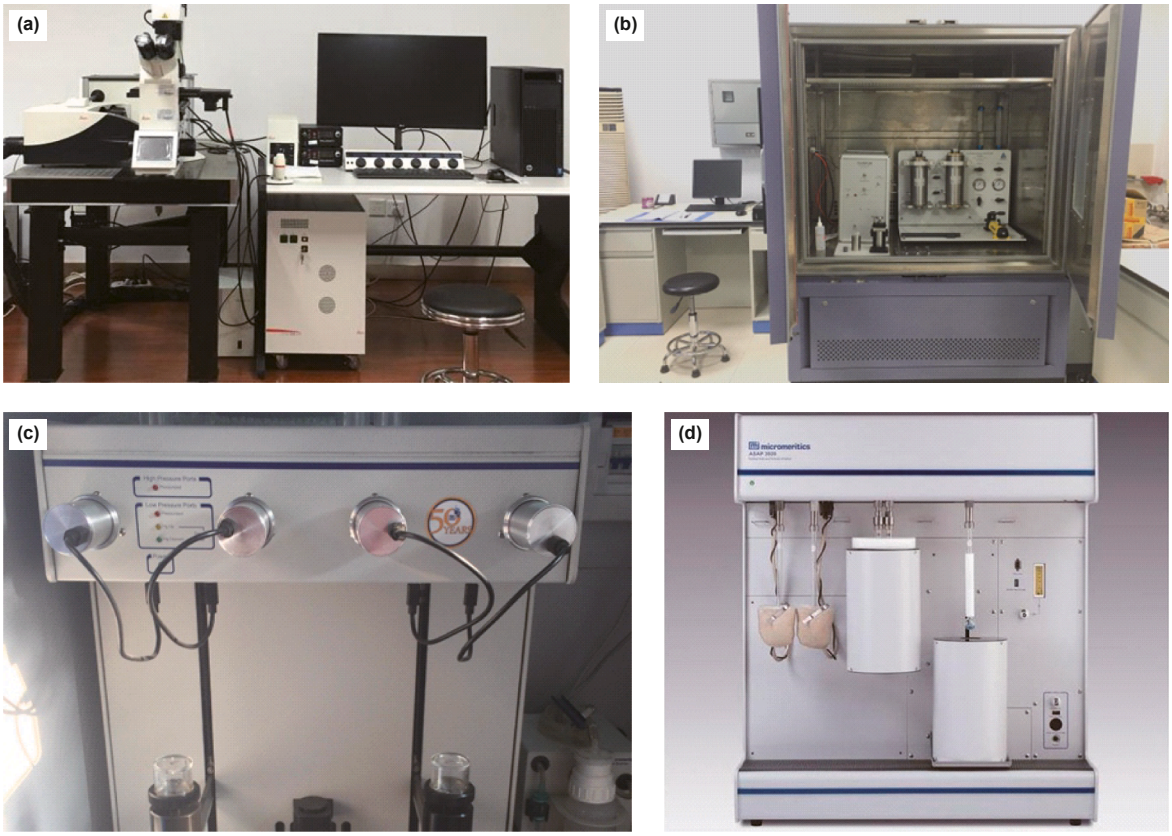

Fig. 2. The mixed sedimentary reservoirs testing equipment utilized in this work. (**a**) LEICA SP5II laser scanning confocal microscope. (**b**) NDP-605 ultra-low permeability and meter helium porosity meter. (**c**) AutoPore 9510-IV instrument. (**d**) ASAP 2460 fully automated surface area and porosity analyzer.

HPMI and LTNA. A higher fractal dimension signifies a more intricate and rougher pore network.

According to Friesen and Mikula (1987) and Broseta et al. (2001), the HPMI fractal dimension D_M can be calculated using the following equation:

$$\ln S_{Hg} = K \times \ln P_c + \ln\alpha \quad (1)$$

$$D_M = K + 2 \quad (2)$$

where S_{Hg} represents the mercury intrusion saturation, %; P_c is the capillary pressure, MPa; α is a proportionality constant; K refers to the slope of the plot of $\ln P_c$ versus $\ln S_{Hg}$.

The LNP fractal dimension D_N is usually calculated using the Frenkel-Halsey-Hill (FHH) model, which is given by the following expression (Avnir and Jaroniec, 1989):

$$\ln V = K \times \ln\left(\ln\left(\frac{P_0}{P}\right)\right) + C \quad (3)$$

$$D_N = K + 3 \quad (4)$$

where V represents the LTNA volume under pressure P, cm^3/g; P_0 is the gas saturation pressure; K refers to the slope of the plot of $\ln V$ versus $\ln(\ln(P_0/P))$.

4. Results and analysis

4.1. Quantitative analyses of pore structure in mixed sedimentary reservoirs

4.1.1. Physical properties

Fig. 3 presents the cross-plot of porosity and permeability obtained from the overburden porosity and permeability tests. The porosity of the samples from the study area varies between 0.40% and 18.60%, with an average of 4.717%. The permeability values mostly range from 0.0145 mD to 0.0551 mD, with an average of 0.0291 mD. These findings indicate that the tight reservoirs in the region are characterized by low porosity and permeability, featuring small pore throats and limited connectivity.

4.1.2. High-pressure mercury injection

HPMI experimental technology provides a direct and quantitative assessment of pore throat size and connectivity. Fig. 4 presents the mercury intrusion and extrusion curves, along with the pore size distribution, for 20 core samples. The detailed data are provided in Table 1.

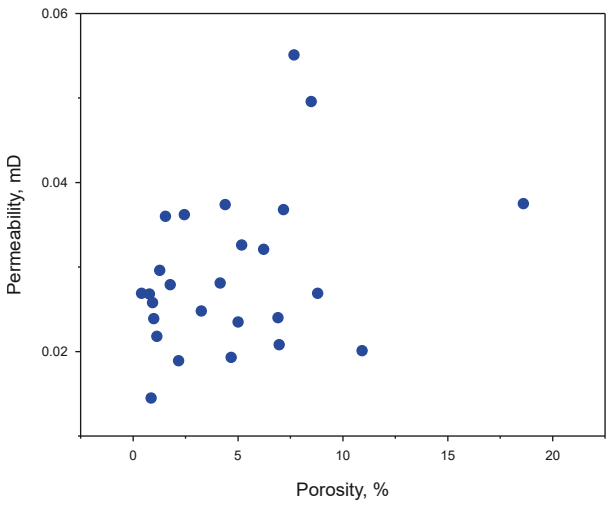

Fig. 3. Porosity and permeability cross plot in mixed sedimentary reservoirs.

The experimental results from HPMI reveal a porosity range of 0.577%–24.438% in the core samples, with an average value of 7.664%. Permeability ranges from 0.0005 mD to 118.90 mD, with a mean of 10.116 mD. The maximum pore throat radius spans from 0.0152 μm to 1.095 μm, with an average of 0.128 μm. Discharge pressure varies between 0.671 MPa and 48.228 MPa, with a mean value of 14.566 MPa. Maximum mercury saturation fluctuates between 87.128% and 97.780%, with an average of 93.079%. Additionally, the mercury removal efficiency shows a range from 13.718% to 91.086%, with a mean of 40.804%. In general, the mixed sedimentary rocks of the Lucaogou Formation are characterized by high displacement pressures and low mercury withdrawal efficiency, which suggests a dense reservoir with poor connectivity.

The mercury intrusion and extrusion curves can be categorized into four distinct types, each corresponding to a different pore-throat combination.

(1) Type I: The mercury injection curve exhibits a weak plateau, characterized by a gently sloping section that extends over a considerable length. This type of reservoir has good porosity and permeability, and low displacement pressure ranging from 0.671 MPa to 5.501 MPa. The pore throat size is relatively large, with the maximum pore throat radius ranging from 0.134 μm to 1.095 μm, and the median radius ranging from 0.035 μm to 0.182 μm. The pore throat size distribution is unimodal, with the pore throat radius of samples 30-1 and 37-1 concentrated at 0.025 μm, while that of samples 31-2 and 43-1 is 0.16 μm.

(2) Type II: The mercury injection curve is characterized by a gentle slope, accompanied by high displacement pressure, ranging from 13.770 MPa to 48.228 MPa. The mercury withdrawal efficiency varies greatly, from 13.718% to 56.837%. The pore throat size distribution is unimodal or bimodal. The unimodal pore size distribution is concentrated at 0.01 μm, while the main peak of the bimodal distribution samples C721 and C571 is 0.1 μm, and the main peak of samples C141, 251-1 and C23 is 0.004 μm.

(3) Type III: The mercury injection curves are characterized by a relatively steep slope, and the mercury withdrawal efficiency is extremely poor, ranging from 14.489% to 24.477%. The pore throat size distribution is unimodal or bimodal, with the main peak located between 0.0063 μm and 0.016 μm.

(4) Type IV: The mercury entry curves are characterized by a gentle slope accompanied by extremely high mercury withdrawal efficiency ranging from 84.154% to 91.086%. The pore throat size distribution is bimodal, with the main peak at 0.004 μm and the secondary peak at 0.04 μm.

4.1.3. Low-temperature nitrogen adsorption

The low-temperature N_2 adsorption/desorption isotherm of the partial sample is depicted in Fig. 5. Based on the IUPAC classification, the N_2 adsorption isotherm predominantly exhibits a type IV pattern, characterized by a pronounced H_3-type hysteresis loop. H_3-type hysteresis loops are typically associated with aggregates of plate-like particles, leading to the formation of narrow, slit-like pores. This observation indicates that slit-like pores are well-developed in the mixed sedimentary reservoirs.

The pore size distribution is typically calculated using N_2 adsorption or desorption data by the Barrett-Joyner-Halenda (BJH) method. However, as highlighted in previous studies, the pore size

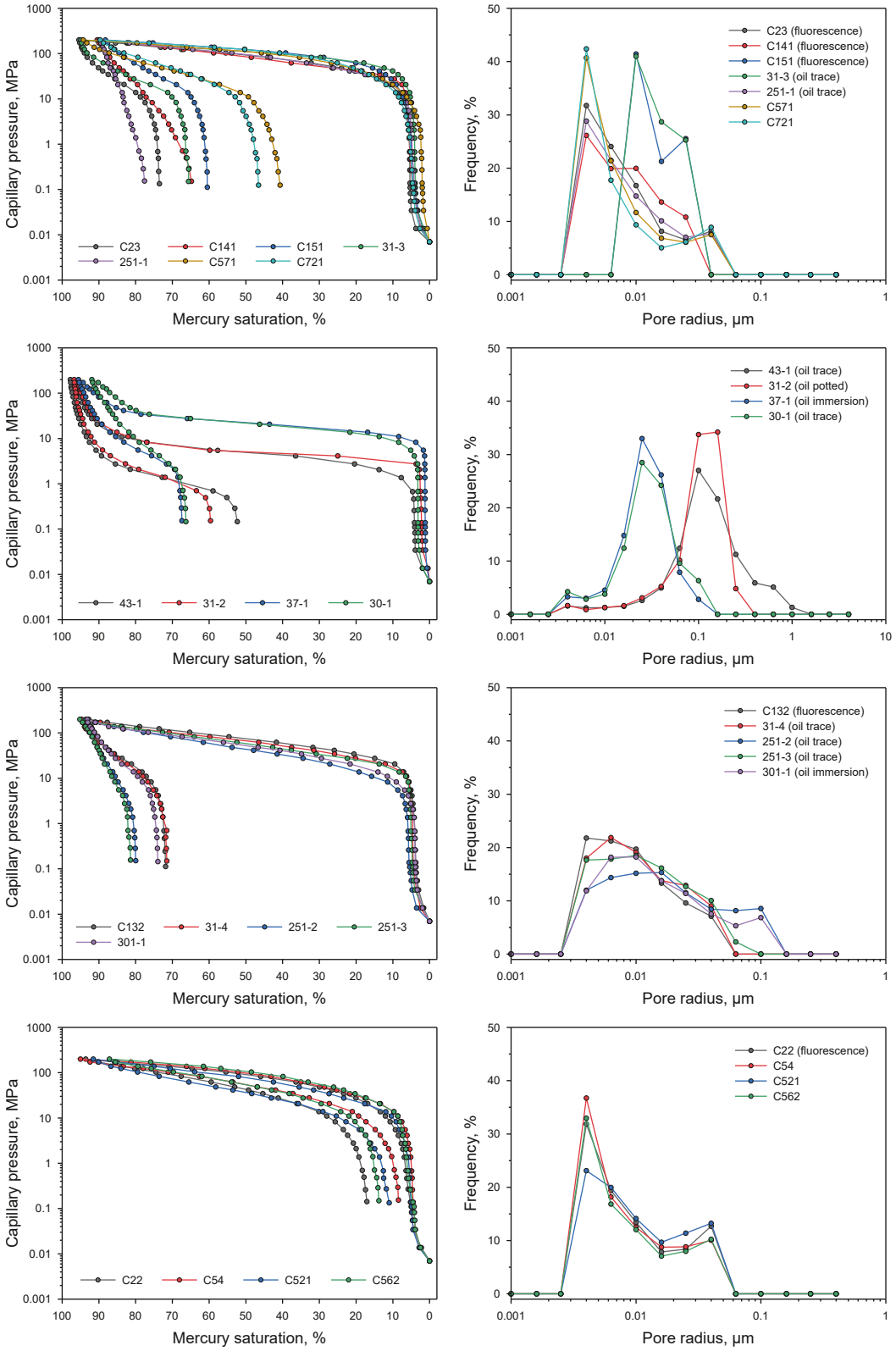

Fig. 4. High-pressure mercury injection curve shape and pore size distribution characteristics in mixed sedimentary reservoirs.

distribution curve obtained from the desorption branch can be influenced by the tensile strength, potentially leading to an inaccurate representation of the actual pore size distribution in porous media (Zou et al., 2015). Therefore, the BJH method was utilized, specifically analyzing data from N_2 adsorption curves, to examine the pore size distribution of samples. The pore volume distribution curves for the selected samples are shown in Fig. 5(b). The pore diameters of these samples display a wide range, spanning from

Table 1
High-pressure mercury injection test data in mixed sedimentary reservoirs.

Curve shape	Sample	Porosity, %	Permeability, mD	Median radius, μm	Discharge pressure, MPa	Maximum pore throat radius, μm	Maximum mercury saturation, %	Efficiency of mercury withdrawal, %
Type I	43-1	24.438	118.900	0.149	0.671	1.095	97.780	46.475
	31-2	21.101	54.800	0.141	2.750	0.267	96.745	38.386
	37-1	18.701	7.507	0.034	5.500	0.134	95.560	29.463
	30-1	10.501	2.571	0.035	5.501	0.134	91.933	27.846
Type II	C23	4.774	0.0005	0.00840	13.770	0.0534	95.440	22.945
	C141	5.154	0.174	0.00897	20.654	0.036	90.482	28.346
	C151	2.745	0.0006	0.00612	48.228	0.0152	88.216	31.407
	31-3	6.426	0.122	0.00681	48.228	0.0152	94.933	30.934
	251-1	6.564	0.150	0.00821	13.776	0.0534	89.941	13.718
	C571	1.851	0.0008	0.00691	13.775	0.0534	94.241	56.837
	C721	1.497	0.0005	0.00615	13.775	0.0534	89.649	48.065
Type III	C132	3.837	0.0011	0.00996	13.793	0.0533	92.770	22.558
	31-4	7.037	0.295	0.0115	13.775	0.0534	94.686	24.477
	251-2	11.450	12.100	0.0172	5.507	0.133	93.540	14.491
	251-3	9.710	0.162	0.0131	11.019	0.0667	95.193	14.489
	301-1	11.853	1.218	0.0143	5.501	0.134	93.175	20.633
Type IV	C22	1.975	0.0005	0.00854	13.769	0.0534	93.603	81.780
	C54	1.425	0.112	0.00799	13.776	0.0534	95.031	91.086
	C521	0.577	0.0007	0.00971	13.771	0.0534	91.524	87.992
	C562	1.672	4.204	0.00722	13.778	0.0533	87.128	84.154

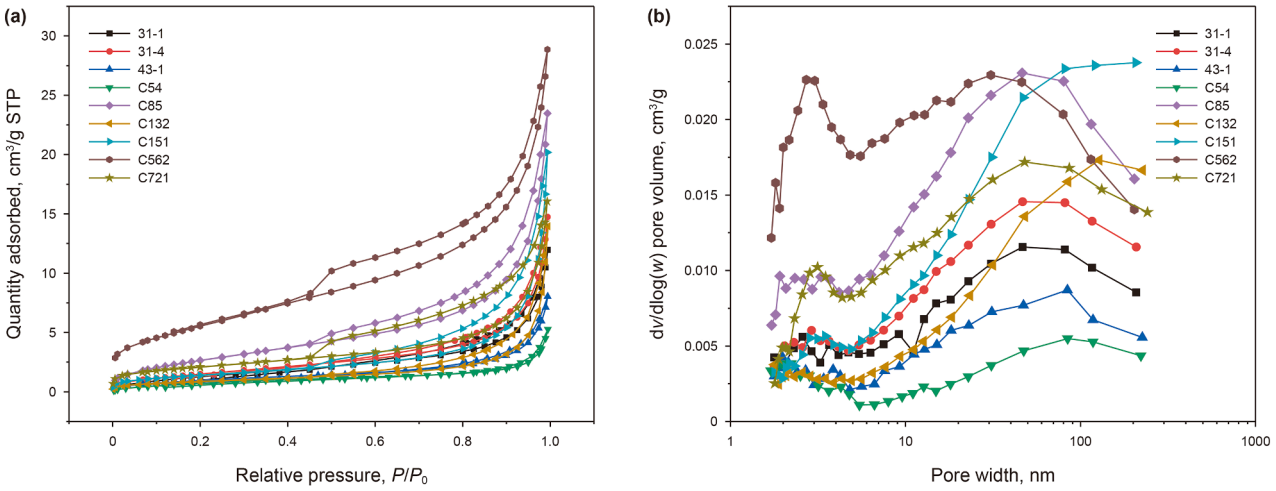

Fig. 5. (**a**) Low-temperature nitrogen adsorption-desorption curve and (**b**) pore diameter distribution curve in mixed sedimentary reservoirs.

1.70 nm to 241.66 nm. Moreover, the pore size distribution curves of most samples are bimodal, with the primary peak occurring around 1.89–3.15 nm and a secondary peak around 30.75–84.58 nm. In contrast, samples C132 and C151 exhibit a unimodal distribution.

The Brunauer-Emmett-Teller (BET) SSA, BJH TPV, BJH average pore diameter (APD), and peak pore diameter distribution (PPDD) were determined from N_2 adsorption data and are summarized in Table 2. The SSA values for all samples vary between 3.155 m^2/g and 20.681 m^2/g, with an average of 7.263 m^2/g. This large SSA

Table 2
Pore structure parameters for low-temperature nitrogen adsorption in mixed sedimentary reservoirs.

Sample	Brunauer-Emmett-Teller specific surface area, m^2/g	Barrett-Joyner-Halenda total pore volume, mm^3/g	Barrett-Joyner-Halenda average pore diameter, nm	Peak pore diameter distribution, nm
31-1	5.351	18.331	13.29	1.89, 84.24
31-4	6.031	22.673	14.59	2.90, 46.69
43-1	3.800	12.392	13.49	1.98, 84.24
C54	3.155	8.025	11.08	2.32, 84.58
C85	10.538	36.309	13.04	1.91, 46.32
C132	3.246	22.295	21.89	127.82
C151	5.085	32.350	19.95	3.49
C562	20.681	44.121	8.81	2.72, 30.75
C721	7.476	25.497	12.72	3.15, 48.00

provides highly favorable conditions for shale oil adsorption. The TPV varies from 0.008025 cm^3/g to 0.044121 cm^3/g, with an average of 0.024666 cm^3/g. Meanwhile, APD spans from 8.81 nm to 21.89 nm, with an average value of 14.32 nm. The PPDD primarily falls within two ranges: 1.89–3.49 nm and 30.75–127.81 nm.

The SSA and TPV of the reservoir are influenced by the micropores (< 2 nm), mesopores (2–50 nm), and macropores (> 50 nm) within the pore network, which are classified according to the IUPAC system. Fig. 6 illustrates the contributions of various pore sizes to both TPV and SSA. Mesopores and macropores are the main contributors to the TPV, whereas micropores contribute minimally. In terms of SSA, mesopores are the absolute contributor, micropores increase their contribution to the SSA compared to their contribution to the TPV, while the contribution of macropores decreases significantly. This indicates that meso-macro pores contribute more to the occurrence of shale oil in the Lucaogou Formation.

Fig. 7 shows the increment curve of the LTNA SSA about pore size. Pores with sizes smaller than 10 nm primarily contribute to the SSA, and the increment curve displays a unimodal pattern. Fig. 8 illustrates the relationship between SSA and TPV. Except for a few outliers, a generally positive correlation is observed between the two parameters, consistent with findings from previous studies on marine and marine-continental transitional shales (Xiong et al., 2015; Li et al., 2019).

4.2. Pore fractal characteristics in mixed sedimentary reservoirs

4.2.1. Fractal characteristics of high-pressure mercury intrusion experiments

The pore space of the shale oil reservoir in the Lucaogou Formation is partitioned using fractal theory, based on the results from HPMI experiments, which aids in classifying reservoir types. In the lg(S_{Hg})–lg(P_c) double logarithmic coordinate system, the mercury injection curve of the core sample exhibits a piecewise straight-line pattern, suggesting that the pore space of the shale oil reservoir displays multiple fractal characteristics (Fig. 9). The fractal dimensions derived from HPMI curves can take two forms: two-stage or three-stage. A fractal dimension greater than 3 is considered meaningless.

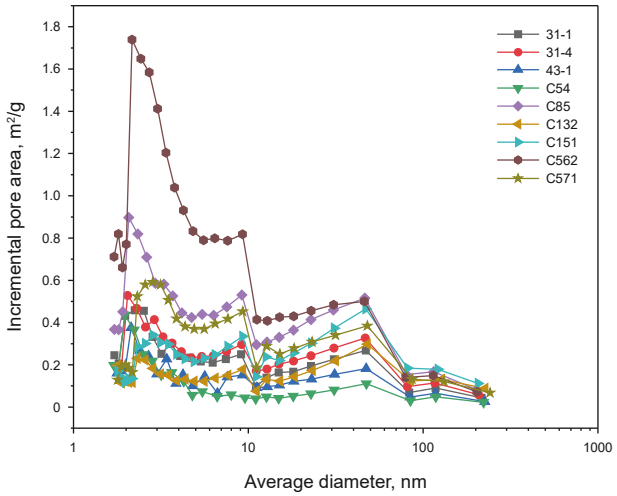

Fig. 7. Relationship between pore size and specific surface area increment derived from low-temperature nitrogen adsorption in mixed sedimentary rock reservoirs.

The fractal dimension D of the two-stage fractal curve is between 2.0366 and 2.9872, with an average of 2.4261 (Table 3). D_{M1} is between 2.694 and 2.9872, with an average of 2.8434. The correlation coefficient (R^2) of the lgP_c and lg(S_{Hg}) curves is between 0.9588 and 0.9989, with an average of 0.9841. D_{M2} is between 2.0366 and 2.1467, with an average of 2.0870. The correlation coefficient (R^2) of the lg(P_c) and lg(S_{Hg}) curves is between 0.8331 and 0.9779, with an average of 0.9214. The fractal dimension D of the three-segment fractal curve ranges from 2.0208 to 2.0836, with an average of 2.0543 (Table 4). D_{M1} is between 2.0375 and 2.0836, with an average of 2.0543. The correlation coefficient (R^2) of the lg(P_c) and lg(S_{Hg}) curves is between 0.8609 and 0.9914, with an average of 0.9383. When D_{M2} is greater than 3, it is meaningless when the fractal dimension is greater than 3. The correlation coefficient (R^2) of the lgP_c and lg(S_{Hg}) curves is between 0.8178 and 0.9855, with an average of 0.9406. D_{M3} is between 2.0208 and 2.0823, with an average of 2.0543. The correlation coefficient (R^2) of the lg(P_c) and lg(S_{Hg}) curves is between 0.6468 and 0.9710, with an average of 0.8866.

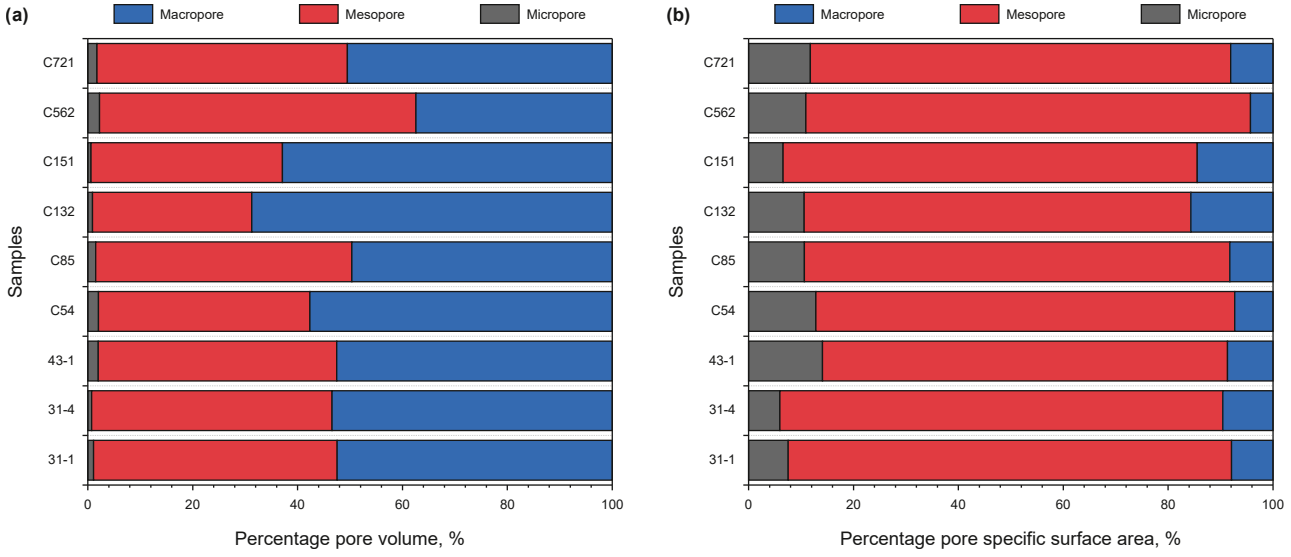

Fig. 6. Pore size distribution at multiple scales derived from low-temperature nitrogen adsorption in mixed sedimentary rock reservoirs: (**a**) percentage of pore volume, (**b**) percentage of pore specific surface area.

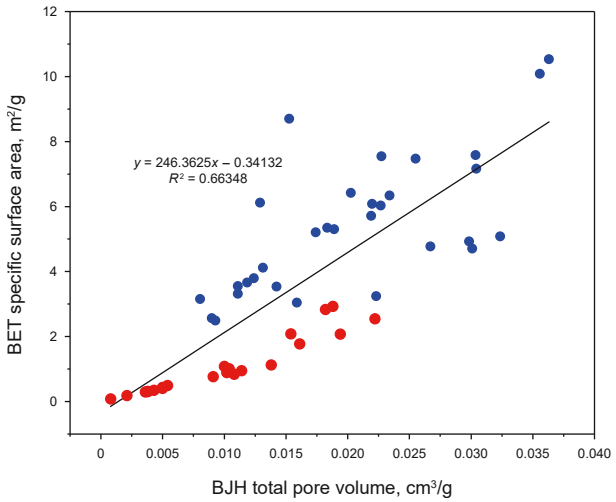

Fig. 8. Relationship between the specific surface area and total pore volume acquired from low-temperature nitrogen adsorption in mixed sedimentary reservoirs (red marked data from Luo et al., 2023).

Table 3
Fractal dimensions of high-pressure mercury injection with two-stage curve in mixed sedimentary reservoirs.

Samples	A_1	R^2	$D_{M1} = 2+A_1$	A_2	R^2	$D_{M2} = 2+A_2$
C23	0.9010	0.9853	2.9010	0.0366	0.8686	2.0366
C141	1.1395	0.9646	3.1395	0.0962	0.9263	2.0962
C151	1.0679	0.9781	3.0679	0.1175	0.9196	2.1175
31-3	1.3276	0.9778	3.3276	0.0605	0.8744	2.0605
251-1	0.9751	0.9945	2.9751	0.0937	0.9319	2.0937
C571	0.8668	0.9870	2.8668	0.1046	0.9329	2.1046
C721	0.8159	0.9765	2.8159	0.1055	0.9517	2.1055
C132	0.9872	0.9825	2.9872	0.0821	0.9335	2.0821
31-4	0.9744	0.9741	2.9744	0.0628	0.8671	2.0628
251-2	0.6940	0.9736	2.694	0.0631	0.9298	2.0631
251-3	0.9475	0.9588	2.9475	0.0534	0.9281	2.0534
301-1	0.7485	0.9846	2.7485	0.0488	0.8331	2.0488
C22	0.7320	0.9931	2.7320	0.1467	0.9675	2.1467
C54	0.7791	0.9917	2.7791	0.0862	0.9644	2.0862
C521	0.7344	0.9922	2.7344	0.0925	0.9358	2.0925
C562	0.8088	0.9989	2.8088	0.1423	0.9779	2.1423

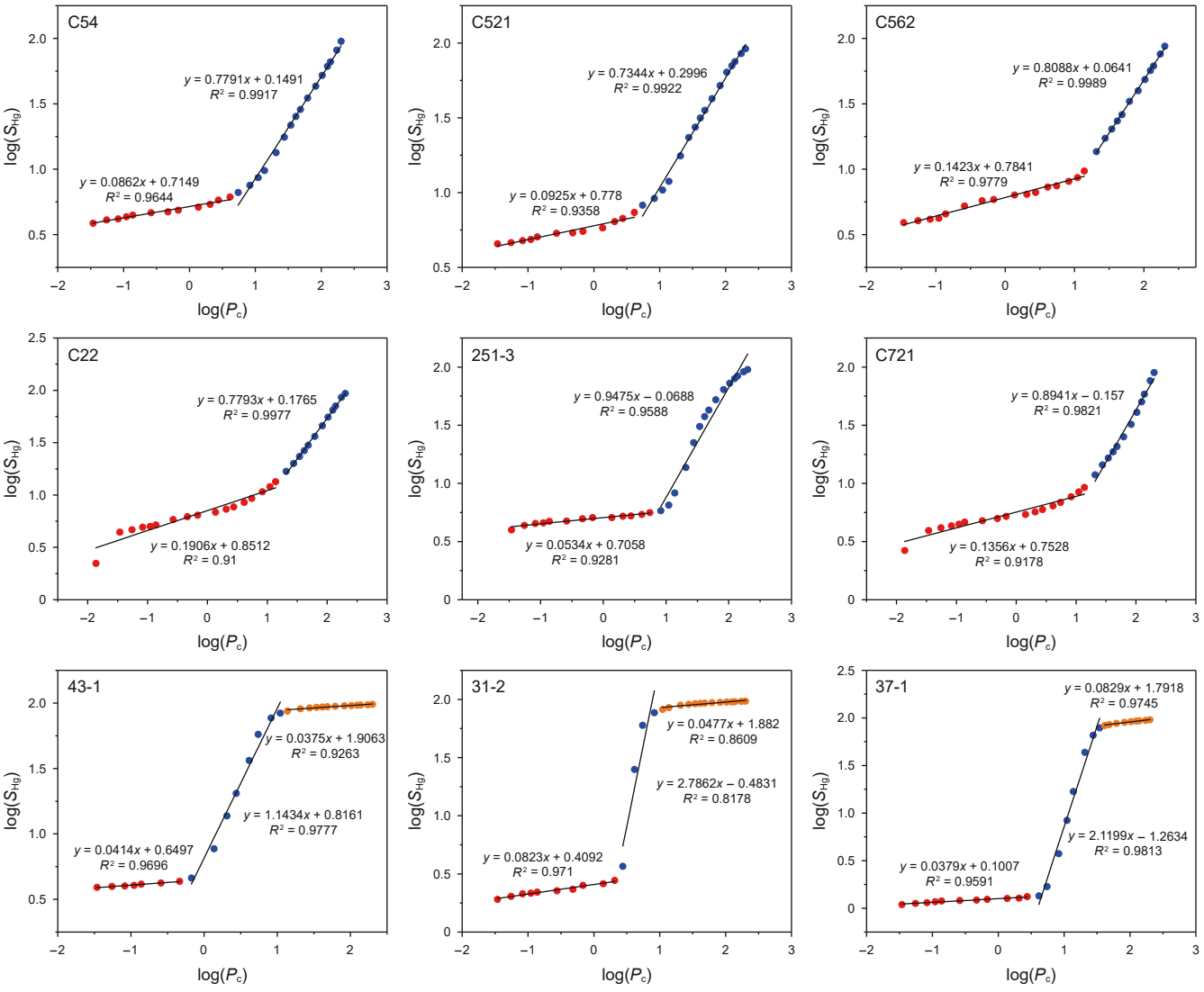

Fig. 9. Log (P_c) and log (S_{Hg}) diagrams reconstructed using high-pressure mercury injection in mixed sedimentary reservoirs.

Table 4
Fractal dimensions of high-pressure mercury injection with three-stage curve in mixed sedimentary reservoirs.

Samples	A_1	R^2	$D_{M1} = 2+A_1$	A_2	R^2	$D_{M2} = 2+A_2$	A_3	R^2	$D_{M3} = 2+A_3$
43-1	0.0375	0.9263	2.0375	1.1434	0.9777	3.1434	0.0414	0.9696	2.0414
31-2	0.0477	0.8609	2.0477	2.7862	0.8178	4.7862	0.0823	0.9710	2.0823
37-1	0.0829	0.9745	2.0829	2.1199	0.9813	4.1199	0.0379	0.9591	2.0379
30-1	0.0836	0.9914	2.0836	1.4937	0.9855	3.4937	0.0208	0.6468	2.0208

4.2.2. Fractal characteristics of low-temperature nitrogen adsorption isotherms

The LTNA and desorption curve shows a hysteresis loop at relative pressures (P/P_0) greater than 0.45. Thus, the adsorption mechanisms differ between the two relative pressure ranges, with distinct behaviors observed for $P/P_0 < 0.45$ and $P/P_0 > 0.45$. For P/P_0 values less than 0.45, the fractal dimension D_{N1} reflects the surface properties of the pore, indicating the impact of van der Waals forces. When P/P_0 exceeds 0.45, the fractal dimension D_{N2} characterizes the internal structure of the pore, which is influenced by the capillary condensation effect (Liang et al., 2015; Cao et al., 2024). Fig. 10 displays the FHH plot of $\ln(V)$ against $\ln(\ln(P_0/P))$ for the sample, derived from LTNA data.

Table 5 presents the linear regression slope, the correlation coefficient (R^2), and the fractal dimension for each sample. The R^2 values exceed 0.93 for all samples, and the fractal dimensions, with one exception, fall within the range of 2–3, suggesting that the pore structures exhibit fractal geometric characteristics. The D_{N1} values range from 2.0768 to 2.4602, with an average of 2.2269. In contrast, the D_{N2} values span from 2.4970 to 2.7283, averaging

Table 5
Fractal dimensions derived from Frenkel-Halsey-Hill model.

Samples	P/P_0: 0–0.45			P/P_0: 0.45–1		
	A_1	R^2	$D_{N1} = 3+A_1$	A_2	R^2	$D_{N2} = 3+A_2$
31-1	−0.9232	0.9936	2.0768	−0.3746	0.9692	2.6254
31-4	−0.7613	0.9879	2.2387	−0.3964	0.9940	2.6036
43-1	−0.8338	0.9620	2.1662	−0.3762	0.9942	2.6238
C54	−1.1144	0.9593	1.8856	−0.3329	0.9932	2.6671
C85	−0.7479	0.9860	2.2521	−0.3812	0.9915	2.6188
C132	−0.7405	0.9443	2.2595	−0.5030	0.9970	2.4970
C151	−0.6948	0.9373	2.3052	−0.5013	0.9975	2.4987
C562	−0.5398	0.9993	2.4602	−0.2717	0.9850	2.7283
C721	−0.6018	0.9344	2.3982	−0.3826	0.9960	2.6174

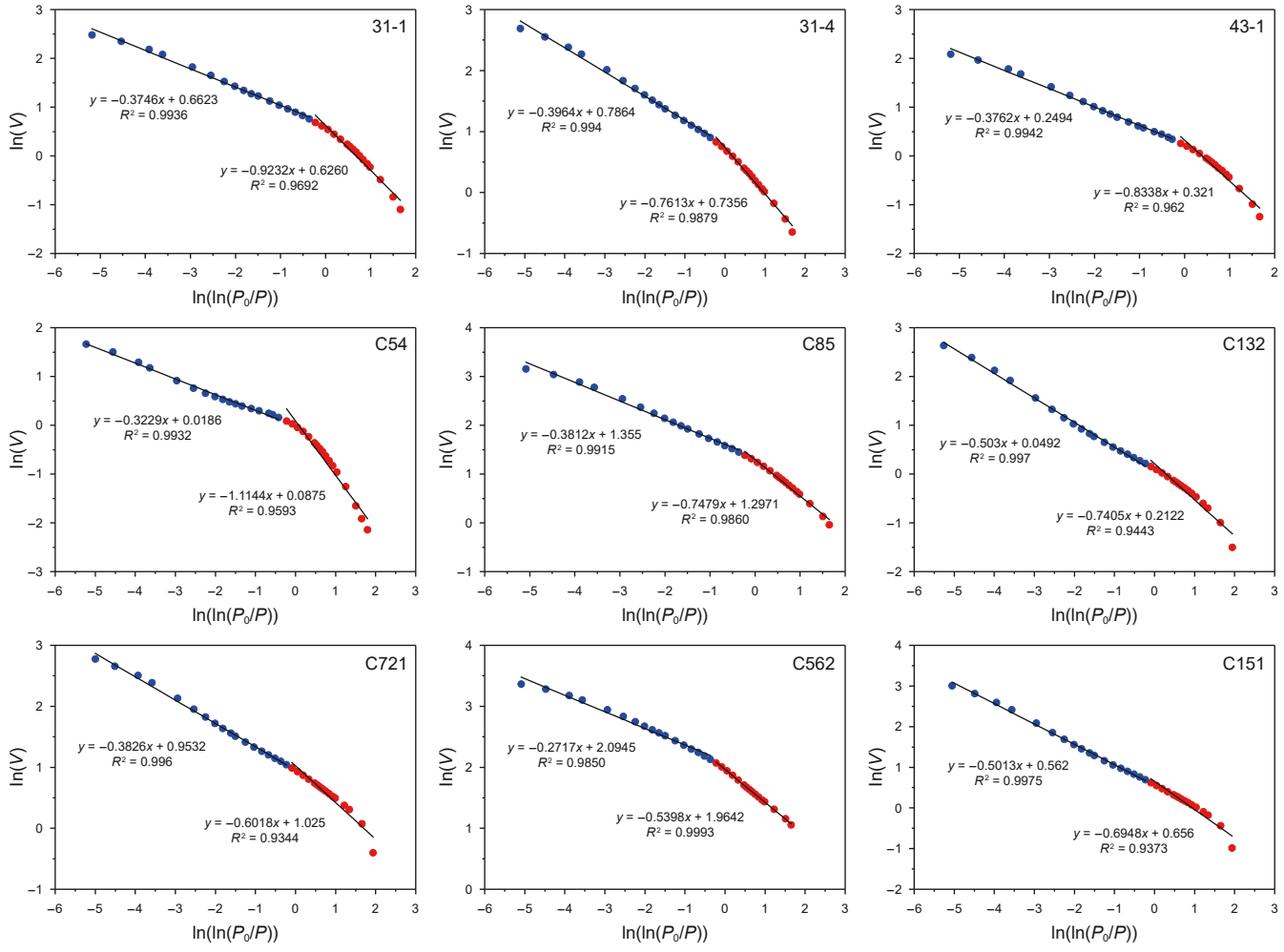

Fig. 10. The $\ln(V)$ and $\ln(\ln(P_0/P))$ diagrams reconstructed using low-temperature nitrogen adsorption in mixed sedimentary reservoirs.

2.6089. The D_{N2} value is observed to be higher than that of D_{N1}, indicating that the internal structure of the pore is more intricate than its surface. Previous research indicates that when the macropore structure is more complex than that of smaller pores, the D_{N2} value exceeds D_{N1}. The complexity of macropore structures arises from the diversity of macropore types, such as intergranular, intragranular, and intercrystalline pores, whereas small pores tend to exhibit a more uniform structure (Yang et al., 2022). A higher pore fractal dimension indicates increased surface roughness and structural complexity of the pores, leading to greater heterogeneity, which is more conducive to shale oil accumulation.

4.3. Hydrocarbon occurrence characteristics in mixed sedimentary reservoirs

Laser confocal fluorescence analysis shows that the heavy components of hydrocarbons are close to the debris particles (Fig. 11(a)), located at the edge of the large pores and in the small pores, and the light components are mainly distributed in the center of the large pores (Fig. 11(b) and (c)). In the field where the relative content ratio of light components to heavy components is 2.0506, the blue heavy components are usually located at the edge of the pore, while in the sample with a light-to-heavy ratio of 0.8182, the light components are mainly located in the center of the pore throat (Fig. 11(d) and (e)).

The light and heavy components in the same pore are distributed differently, with the light components distributed in the center of the pore and the heavy components distributed around the pore and wrapping the light components. Zhang et al. (2019) used molecular dynamics simulation to reveal that the density of crude oil gradually decreases from the pore wall to the center of the pore. The high-density heavy oil is mostly adsorbed on the surface of the pore wall, while the light oil in the center of the pore is free, which is consistent with the results observed by LSCM (Sun et al., 2005).

5. Discussion

5.1. Relationship between pore fractal dimension and pore structure parameters in mixed sedimentary reservoirs

Fig. 12 shows the relationship between pore structure parameters and LTNA fractal dimension. Compared with D_{N1}, the BET SSA shows a weak positive correlation ($R^2 = 0.11099$) with D_{N2}, indicating that for the pore surface, the heterogeneity of the pore structure of the entire reservoir controls the SSA. The stronger the heterogeneity, the higher the SSA (Fig. 12(a)). This is contrary to previous studies on transitional shale (Li et al., 2019). With the increase of D_{N2}, the BJH TPV shows an increasing trend (Fig. 12(b)). The positive correlation ($R^2 = 0.3620$) between D_{N1} and the BJH TPV means that the surface roughness of micropores and mesopores is conducive to the TPV. D_{N2}, which represents the complexity of the reservoir pore space, has little effect on the growth of TPV. The BJH APD of the reservoir shows a strong negative correlation with D_{N2} ($R^2 = 0.93242$), suggesting that an increase in the complexity of the pore network corresponds to a decrease in the average pore size (Fig. 12(c)).

Fig. 13 illustrates an inverse relationship between porosity and the fractal dimension of macropores in the shale oil reservoir. As porosity rises, the fractal dimension of the macropores decreases and remains below 2.5. This indicates that a more intricate macropore structure is associated with increased heterogeneity, which subsequently restricts the development of the reservoir's porosity.

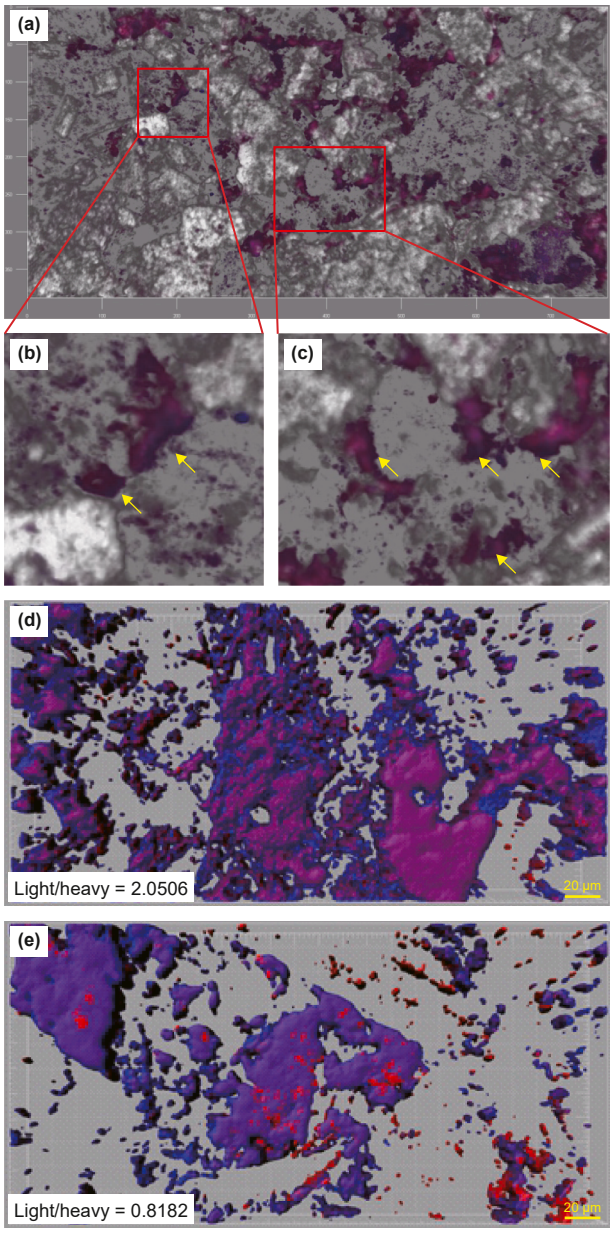

Fig. 11. (**a**) Distribution of crude oil components under laser confocal fluorescence microscopy in mixed sedimentary reservoirs (red is light components, blue is heavy components, and white is transparent minerals). (**b**) and (**c**) Enlarged images of the local area of (a). (**d**) Three-dimensional fluorescence modeling image with a light component to heavy component ratio of 2.0506. (**e**) Three-dimensional fluorescence modeling image with a light component to heavy component ratio of 0.8182.

5.2. Fractal characteristics of pore structures in mixed sedimentary rock reservoirs and their implications for shale oil accumulation

The oil content in the cores from the Lucaogou Formation in the Jimusar Sag shows significant variability. These cores exhibit different oil-bearing categories, as shown in Fig. 14, including fluorescence, oil traces, oil spots, and oil-impregnated types. A clear increase in oil content occurs as the grade transitions from fluorescent to oil-impregnated. Notably, higher porosity promotes greater oil content (Fig. 14(a)), with samples containing oil traces, oil spots, and oil leaching showing significantly higher porosity compared to the fluorescent samples (Fig. 14(a)). This observation

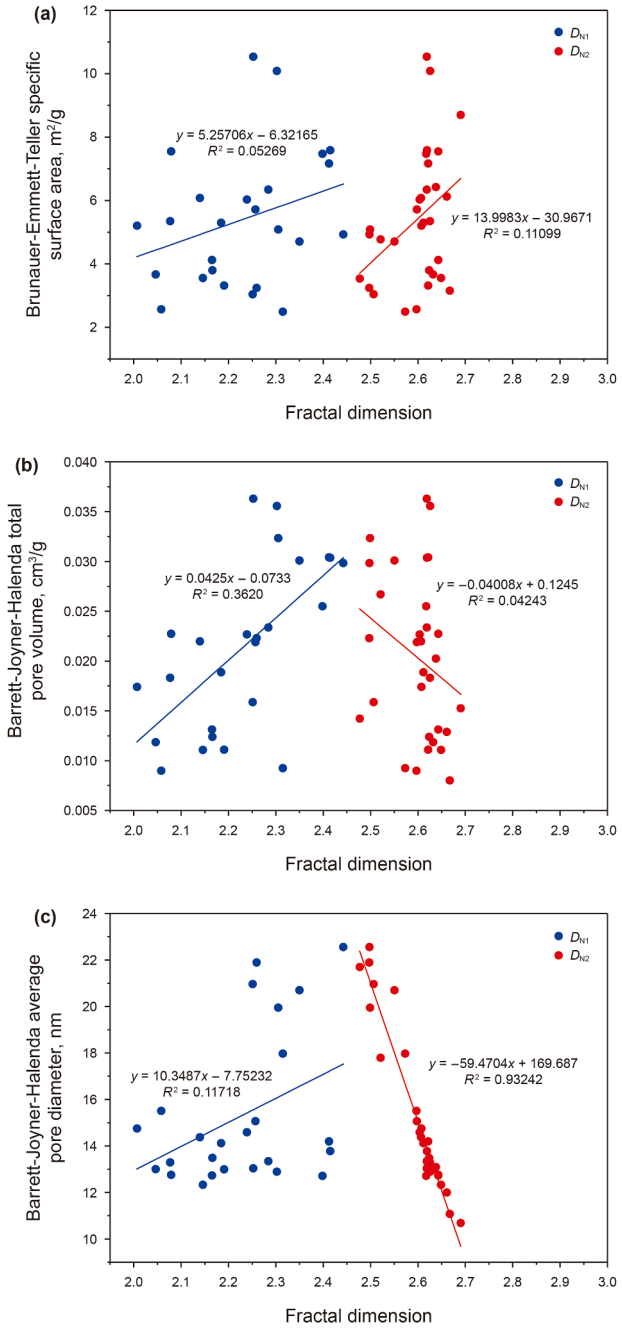

Fig. 12. Relationship between pore fractal dimensions (D_{N1} and D_{N2}) and pore structure parameters in mixed sedimentary reservoirs. (**a**) Brunauer-Emmett-Teller specific surface area; (**b**) Barrett-Joyner-Halenda total pore volume; (**c**) Barrett-Joyner-Halenda average pore diameter.

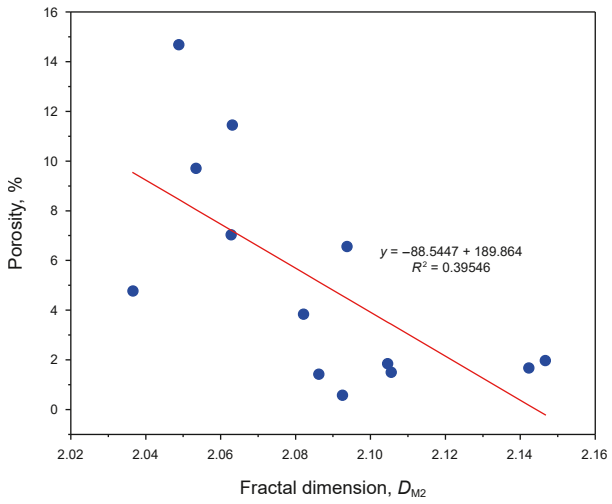

Fig. 13. Relationship between porosity and fractal dimension (D_{M2}) in mixed sedimentary reservoirs.

suggests that the physical properties of the reservoir play a crucial role in influencing oil aggregation.

The fractal dimension exhibits a strong correlation with the petrophysical properties of shale oil reservoirs in the Lucaogou Formation of the Jimusar Sag. Reservoir samples that display high porosity, larger pore-throat radii, enhanced connectivity between pore throats, and improved sorting generally show lower fractal dimensions. As a result, fractal characteristics serve as a comprehensive indicator of the reservoir's nanopore structure, representing a key factor in hydrocarbon accumulation. Fig. 14(b) illustrates that the fractal dimension of smaller pores decreases as oil content increases, whereas the fractal dimension of larger pores remains largely unchanged (Fig. 14(c)). This suggests that the fractal features of smaller pores exert a more pronounced influence on oil content, with the structural complexity of small pores playing a pivotal role in the accumulation of shale oil.

5.3. Microscopic occurrence mechanism of shale oil in mixed sedimentary reservoirs

Previous studies on the occurrence of hydrocarbons have mainly focused on the oil-water relationship of macroscopic reservoirs, and the microscopic occurrence of hydrocarbons in micron-nanoscale pore throats of shale oil has not been extensively studied (Wu et al., 2021; Zhang et al., 2023a). This study conducted laser confocal microscopic fluorescence analysis on the oil-rich core of the Lucaogou Formation (Fig. 15(a)) and found that the heavy components were close to the edge of the particles, while the light components were located in the center of the

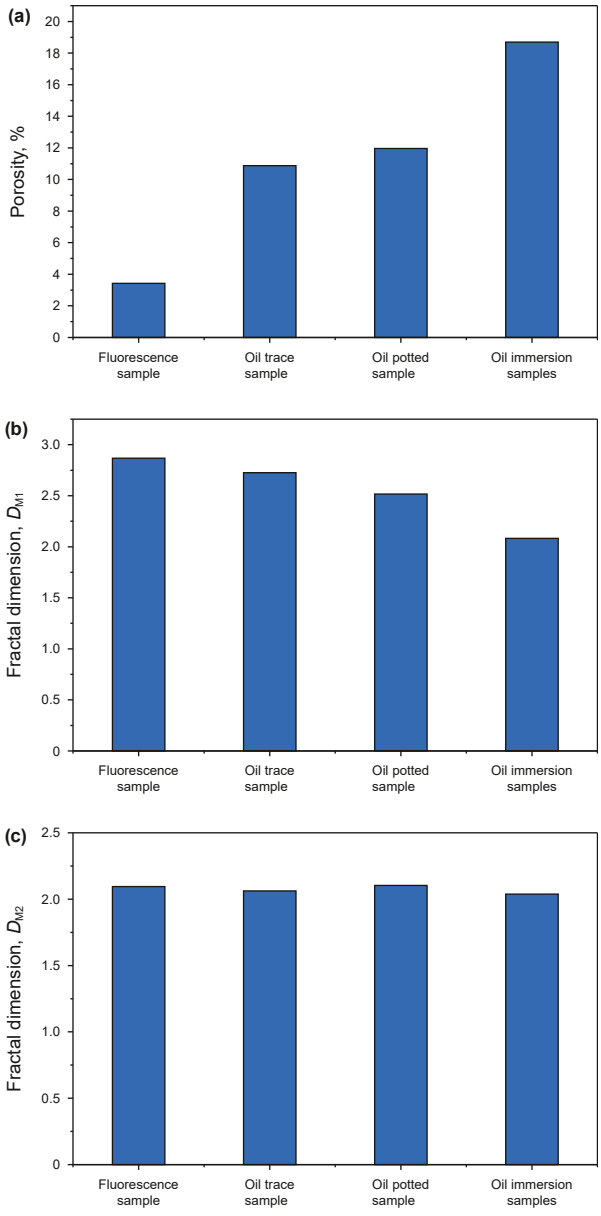

Fig. 14. Correlation between oil content grade, porosity, and fractal dimensions (D_{M1} and D_{M2}) in mixed sedimentary reservoirs.

particles (Fig. 15(b) and (c)). The occurrence characteristics of light and heavy components are mainly affected by two key mechanisms: the coupling control effect of crude oil charging force and capillary resistance, and the adsorption effect of reservoir minerals (Jiang et al., 2025). First, crude oil charging force and pore capillary resistance jointly determine the preservation of light and heavy components in pores. When the hydrocarbon generation intensity is large enough, the crude oil charging force makes this coupling control not obvious for the difference between light and heavy crude oils (Fig. 11(d)). However, for most reservoirs, due to insufficient oil and gas charging force, the capillary resistance of crude oil rich in light components is weaker than that of crude oil rich in heavy components, so it is easier to be differentiated and to exist in smaller pores. (Fig. 11(e)). In addition, the oil saturation of the reservoir is generally low, and the adsorption of crude oil by minerals under the coexistence of oil and water also controls the differential distribution of light and heavy components. Due to its higher polarity and molecular weight, the adsorption force of heavy components on the mineral surface is stronger than that of light components, so it is easier to exist on the pore surface.

The mudstone of the Lucaogou Formation in the Jimusar Sag is very developed. Due to the high initial porosity of the mudstone during the sedimentary period, generally exceeding 60%, the pores are rich in water. Therefore, during the burial compaction process, mudstone compression centrifugal flow occurs. In the shallow burial stage before organic matter generates hydrocarbons, the fluid stored in the reservoir is mainly formation water formed by compression centrifugal flow. As the burial depth increases, the organic matter enters the early maturity stage. The hydrocarbons discharged in the early stage are generally larger in molecular weight and have more polar components. Therefore, the heavy components in the hydrocarbons in the early accumulation stage are relatively high. When they are injected into the reservoir, they are easily adsorbed by particles and located at the edge of the pores. As the burial depth increases, the hydrocarbons generated by organic matter are mainly low-molecular-weight hydrocarbons, so the late accumulation is mainly light components. During the migration of hydrocarbons, they often follow the direction of least resistance. Therefore, the light component hydrocarbons generated in the late stage will occupy the center of the pores. Therefore, reservoirs with higher oil saturation exhibit a distribution pattern of clay film–heavy components–light components–water, progressing from the edge of the detrital grain to the center of the pore (Fig. 15(d) and (e)).

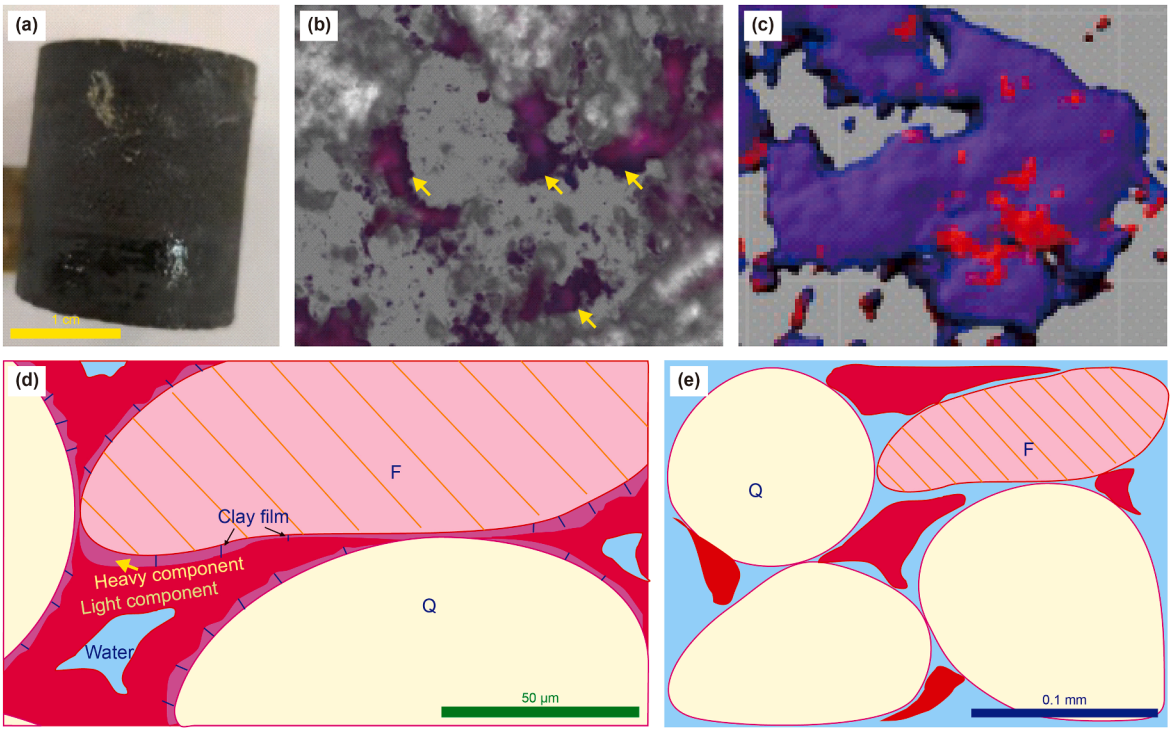

Fig. 15. Hydrocarbon occurrence states and conceptual model in mixed sedimentary reservoirs.

6. Conclusions

The status of shale oil in oil exploration and development is becoming increasingly prominent. Shale oil is mainly found in the micro-nano pore structure of reservoirs, and its resources and development require in-depth research. The micro-nanostructure of the mixed sedimentary reservoir of the Lucaogou Formation was systematically characterized by high-pressure mercury injection, low-temperature nitrogen adsorption, laser scanning confocal microscopy experiments and fractal theory, providing new insights into the microscopic enrichment model of shale oil. The conclusions reached are as follows:

(1) The physical properties and micro-nano pore structure parameters of the mixed sedimentary reservoir were obtained. The porosity is mainly 0.40%–18.60%, and the permeability is between 0.145 mD and 0.0551 mD. The pore type is slit-like shaped, and the pore size distribution of most mixed sediments is bimodal, with a smaller peak ranging from 1.89 nm to 3.15 nm and a larger peak ranging from 30.75 nm to 84.58 nm. Mesopores and macropores contribute the majority of TPV, while mesopores are the bulk of SSA. The pore throat structure of the reservoir can be divided into four types.

(2) The influence of the fractal dimension of the mixed sedimentary reservoir on the pore structure parameters is investigated. The pore fractal dimensions ranged from 2.1662 to 2.6254 for D_{N1} and 2.0768 to 2.7283 for D_{N2}. The complexity of the macropore structure increases, and the average pore size decreases. The porosity of shale oil reservoirs is inversely proportional to the fractal dimension of macropores (D_{M2}), indicating that the complexity and increased heterogeneity of the macropore structure hinder the development of reservoir porosity and are not conducive to the development of effective porosity.

(3) The controlling mechanism of oil accumulation in mixed sedimentary reservoirs is discussed. The accumulation of shale oil is significantly affected by reservoir physical properties, and high reservoir porosity is conducive to the increase of oil content. The fractal characteristics of small pores (2.32–36.90 nm) exert significant control on shale oil accumulation. The control mechanism of pores on oil content can assist in the selection of favorable areas for shale oil.

(4) The enrichment pattern of shale oil in mixed rock reservoirs was revealed. The coupling of charging force and pore capillary resistance controls the enrichment pattern of light components in the pore center and heavy components in the pore edge. In reservoirs with high oil saturation, the distribution sequence from the edge of the rock particles to the pore center follows the order of clay film, heavy components, light components, and water. The occurrence mechanism can predict the sweet spot area more accurately in shale oil exploration and development, optimize the well location layout and formulate targeted oil displacement designs. The identification of pore networks aims to provide valuable information for fracturing production enhancement strategies that improve oil flow paths and enhance oil recovery. Overall, the results are conducive to conducting reservoir evaluation and development planning of shale oil reservoirs more effectively.

CRediT authorship contribution statement

Lei Xiao: Writing – original draft, Software, Methodology, Investigation, Formal analysis. **Yi-Wen Ju:** Writing – review & editing, Supervision, Project administration, Funding acquisition, Conceptualization. **Jun Jin:** Writing – review & editing. **Jin Liu:** Writing – review & editing. **Jing-Qiang Tan:** Writing – review & editing. **Shu Jiang:** Writing – review & editing. **Xin Li:** Writing –

review & editing. **Bing Hou:** Writing – review & editing. **Peng Qiao:** Writing – review & editing. **Xin-Gao Hou:** Writing – review & editing. **Jian Gao:** Writing – review & editing.

Declaration of competing interests

The authors declare that they have no known competing financial interests or personal relationships that could have appeared to influence the work reported in this paper.

Acknowledgements

This research was financially supported by the National Natural Science Foundation of China (Grant Nos. 42372153, 41530315) and the research program of the PetroChina Xinjiang Oilfield Company (Grant No. 2018-C4035).

References

Adeyilola, A., Nordeng, S., Hu, Q., 2022. Porosity and pore networks in tight dolostone—Mudstone reservoirs: Insights from the Devonian three forks formation, Williston Basin, USA. J. Earth Sci. 33 (2), 462–481. https://doi.org/10.1007/s12583-021-1458-3.

Avnir, D., Jaroniec, M., 1989. An isotherm equation for adsorption on fractal surfaces of heterogeneous porous materials. Langmuir 5, 1431–1433. https://doi.org/10.1021/la00090a032.

Broseta, D., Barré, L., Vizika, O., et al., 2001. Capillary condensation in a fractal porous medium. Phys. Rev. Lett. 86, 5313. https://doi.org/10.1103/PhysRevLett.86.5313.

Bu, H.L., Ju, Y.W., Tan, J.Q., et al., 2015. Fractal characteristics of pores in non-marine shales from the Huainan coalfield, Eastern China. J. Nat. Gas Sci. Eng. 24, 166–177. https://doi.org/10.1016/j.jngse.2015.03.021.

Cao, Y., Jin, Z.J., Zhu, R.K., et al., 2024. Pore systems and their correlation with oil enrichment in various lithofacies of saline lacustrine shale strata. Int. J. Coal Geol. 282, 104444. https://doi.org/10.1016/j.coal.2024.104444.

Friesen, W.I., Mikula, R.J., 1987. Fractal dimensions of coal particles. J. Colloid Interface Sci. 120 (1), 263–271. https://doi.org/10.1016/0021-9797(87)90348-1.

García-Hidalgo, J.F., Gil, J., Segura, M., et al., 2007. Internal anatomy of a mixed siliciclastic–carbonate platform: The late Cenomanian–mid Turonian at the southern margin of the Spanish central system. Sedimentology 54 (6), 1245–1271. https://doi.org/10.1111/j.1365-3091.2007.00880.x.

Hopkins, A.S., 2017. The next energy economy. Science 356 (6339), 709. https://doi.org/10.1126/science.aam8696.

Hou, L.H., Luo, X., Zhao, Z.Y., et al., 2021. Identification of oil produced from shale and tight reservoirs in the Permian Lucaogou Shale sequence, Jimusar Sag, Junggar Basin, NW China. ACS Omega 6 (3), 2127–2142. https://doi.org/10.1021/acsomega.0c05224.

Jarvie, D.M., 2014. Components and processes affecting producibility and commerciality of shale resource systems. Geol. Acta 12 (4), 307–325. https://doi.org/10.1344/GeologicaActa2014.12.4.3.

Jiang, Y.Q., Liu, Y.Q., Yang, Z., et al., 2015. Characteristics and origin of tuff-type tight oil in Jimusar Sag, Junggar Basin, NW China. Petrol. Explor. Dev. 42 (6), 810–818. https://doi.org/10.1016/S1876-3804(15)30077-X.

Ju, Y.W., Wang, G.Z., Li, S.Z., et al., 2022. Geodynamic mechanism and classification of basins in the Earth system. Gondwana Res. 102, 200–228. https://doi.org/10.1016/j.gr.2020.08.017.

Jiang, M.Y., Chen, D.X., Wang, Q.C., et al., 2025. Occurrence mechanism of crude oil components in tight reservoirs: A case study of the Chang 7 tight oil in the Jiyuan Area, Ordos Basin, China. Energies 18, 1440. https://doi.org/10.3390/en18061440.

Körmös, S., Varga, A., Raucsik, B., 2023. Reservoir heterogeneity of an Eocene mixed siliciclastic–carbonate succession, northern Pannonian Basin. Mar. Petrol. Geol. 147, 105984. https://doi.org/10.1016/j.marpetgeo.2022.105984.

Kuang, L.C., Tang, Y., Lei, D.W., et al., 2012. Formation conditions and exploration potential of tight oil in the Permian saline lacustrine dolomitic rock, Junggar Basin, NW China. Petrol. Explor. Dev. 39 (6), 657–667. https://doi.org/10.1016/S1876-3804(12)60095-0.

Li, P., Zheng, M., Bi, H., et al., 2017. Pore throat structure and fractal characteristics of tight oil sandstone: A case study in the Ordos Basin, China. J. Pet. Sci. Eng. 149, 665–674. https://doi.org/10.1016/j.petrol.2016.11.015.

Li, T.J., Huang, Z.L., Feng, Y., et al., 2020. Reservoir characteristics and evaluation of fluid mobility in organic-rich mixed siliciclastic–carbonate sediments: A case study of the lacustrine Qiketai Formation in Shengbei Sag, Turpan-Hami Basin, Northwest China. J. Pet. Sci. Eng. 185, 106667. https://doi.org/10.1016/j.petrol.2019.106667.

Li, T.J., Huang, Z.L., Zhao, J., et al., 2021. Pore structure characteristics and their influencing factors: A case study from the Middle Jurassic mixed siliciclastic carbonate rocks, Turpan-Hami basin, Northwest China. J. Pet. Sci. Eng. 203, 108611. https://doi.org/10.1016/j.petrol.2021.108611.

Li, Y., Wang, Z.S., Pan, Z.J., et al., 2019. Pore structure and its fractal dimensions of transitional shale: A cross-section from east margin of the Ordos Basin, China. Fuel 241, 417–431. https://doi.org/10.1016/j.fuel.2018.12.066.

Liang, L.X., Xiong, J., Liu, X.J., et al., 2015. An investigation of the fractal characteristics of the Upper Ordovician Wufeng Formation shale using nitrogen adsorption analysis. J. Nat. Gas Sci. Eng. 27, 402–409. https://doi.org/10.1016/j.jngse.2015.07.023.

Lin, M.R., Xi, K.L., Cao, Y.C., et al., 2021. Petrographic features and diagenetic alteration in the shale strata of the Permian Lucaogou Formation, Jimusar Sag, Junggar Basin. J. Pet. Sci. Eng. 203, 108684. https://doi.org/10.1016/j.petrol.2021.108684.

Liu, G., Wang, G.Z., Li, N., et al., 2024. Characteristics and geological significance of carbon and oxygen isotopes of the Permian Lucaogou Formation dolomite in the southern Junggar Basin, Northwestern China. J. Palaeogeogr. 13 (4), 862–882. https://doi.org/10.1016/j.jop.2024.08.008.

Liu, J., Wang, J., Ma, X., et al., 2023. Pore characteristics and genesis of shale oil sweet spots in saline lacustrine basins: A case study from the Lucaogou Formation in the Junggar Basin. Acta Geol. Sin. 97 (3), 864–878. https://doi.org/10.19762/j.cnki.Dizhixuebao.2023217 (in Chinese).

Liu, Y.Z., Zeng, J.H., Yang, G.Q., et al., 2021. An innovative method for the characterization of oil content in lacustrine shale-oil systems: A case study from the Middle Permian Lucaogou Formation in the Jimusar Sag, Junggar Basin. Mar. Petrol. Geol. 130, 105112. https://doi.org/10.1016/j.marpetgeo.2021.105112.

Liu, Y.S., Dong, X.H., Yan, L., et al., 2019. Quantitative characterization of pore structure of lucaogou Formation in Jimsar Sag. Xinjiang Pet. Geol. 40 (3), 284–289. https://doi.org/10.7657/XJPG20190305 (in Chinese).

Luo, J.C., Tian, J.J., He, X.B., et al., 2023. Characteristics and controlling factors of meso-macropore pore structure of Permian Lucaogou Formation reservoir in Jimsar Sag, Junggar Basin. Chin. J. Geol. 58 (3), 1008–1029. https://doi.org/10.12017/dzkx.2023.055 (in Chinese).

Lü, Z.X., Zhang, S.L., Yin, C., et al., 2017. Features and genesis of Paleogene high-quality reservoirs in lacustrine mixed siliciclastic–carbonate sediments, central Bohai Sea, China. Pet. Sci. 14, 50–60. https://doi.org/10.1007/s12182-016-0147-9.

Mandelbrot, B., 1967. How long is the coast of Britain? Statistical self-similarity and fractional dimension. Science 156 (3775), 636–638. https://doi.org/10.1126/science.156.3775.636.

Mcmahon, T.P., Larson, T.E., Zhang, T., et al., 2024. Geologic characteristics, exploration and production progress of shale oil and gas in the United States: An overview. Petrol. Explor. Dev. 51 (4), 925–948. https://doi.org/10.1016/S1876-3804(24)60516-1.

Pan, Y.S., Huang, Z.L., Li, T.J., et al., 2021. Pore structure characteristics and evaluation of lacustrine mixed fine-grained sedimentary rocks: A case study of the Lucaogou Formation in the Malang Sag, Santanghu Basin, Western China. J. Pet. Sci. Eng. 201, 108545. https://doi.org/10.1016/j.petrol.2021.108545.

Pang, X.J., Wang, G.W., Kuang, L.H., et al., 2022. Insights into the pore structure and oil mobility in fine-grained sedimentary rocks: The Lucaogou Formation in Jimusar Sag, Junggar Basin, China. Mar. Petrol. Geol. 137, 105492. https://doi.org/10.1016/j.marpetgeo.2021.105492.

Palermo, D., Aigner, T., Geluk, M., et al., 2008. Reservoir potential of a lacustrine mixed carbonate/siliciclastic gas reservoir: The Lower Triassic Rogenstein in the Netherlands. J. Petrol. Geol. 31 (1), 61–96. https://doi.org/10.1111/j.1747-5457.2008.00407.x.

Qian, X.K., Lu, R.Q., Luo, L.C., et al., 2024. Global oil and gas industry in 2023 and outlook for 2024. Int. Petrol. Econ. 32 (2), 1–13 (in Chinese).

Qu, C.S., Qiu, L.W., Cao, Y.C., et al., 2017. Organic petrology characteristics and occurrence of source rocks in Permian Lucaogou Formation, Jimsar sag. J. China Univ. Pet. 41 (2), 30–38. https://doi.org/10.3969/j.issn.1673-5005.2017.02.004 (in Chinese).

Qu, C.S., Qiu, L.W., Cao, Y.C., et al., 2019. Sedimentary environment and the controlling factors of organic-rich rocks in the Lucaogou Formation of the Jimusar Sag, Junggar Basin, NW China. Pet. Sci. 16, 763–775. https://doi.org/10.1007/s12182-019-0353-3.

Su, Y., Zha, M., Ding, X., et al., 2018. Pore type and pore size distribution of tight reservoirs in the Permian Lucaogou Formation of the Jimsar Sag, Junggar Basin, NW China. Mar. Petrol. Geol. 89, 761–774. https://doi.org/10.1016/j.marpetgeo.2017.11.014.

Sun, X.D., Suo, L.M., Zhang, M.Z., et al., 2005. New progress of reservoir research by the technology of Laser Confocal Scanning Microscope analysis in the Daqing exploration area. Acta Petrol. Sin. 21, 1479–1488 (in Chinese).

Wang, Q., Song, X.X., Li, R.R., 2018. A novel hybridization of nonlinear grey model and linear ARIMA residual correction for forecasting U.S. shale oil production. Energy 165, 1320–1331. https://doi.org/10.1016/j.energy.2018.10.032.

Wang, J., Cao, Y., Liu, K., et al., 2019. Fractal characteristics of the pore structures of fine-grained, mixed sedimentary rocks from the Jimsar Sag, Junggar Basin: Implications for lacustrine tight oil accumulations. J. Pet. Sci. Eng. 182, 106363. https://doi.org/10.1016/j.petrol.2019.106363.

Wang, X.L., Zhang, G.S., Tang, W., 2022a. A review of commercial development of continental shale oil in China. Energy Geosci. 3 (3), 282–289. https://doi.org/10.1016/j.engeos.2022.03.006.

Wang, L.S., Ye, Y.P., Qin, J.H., et al., 2022b. Microscopic pore structure characterization and oil-bearing property evaluation of lacustrine shale reservoir: A case study of the Permian Lucaogou Formation in Jimsar Sag, Junggar Basin. Oil Gas Geol. 43 (1), 149–160. https://doi.org/10.11743/ogg20220112 (in Chinese).

Washburn, E.W., Fooyitt, F.F., 1921. Porosity: III. Water as an absorption liquid. J. Am. Ceram. Soc. 4 (12), 961–982. https://doi.org/10.1111/j.1151-2916.1921.tb18111.x.
Wu, T., Pan, Z., Liu, B., et al., 2021. Laboratory characterization of shale oil storage behavior: A comprehensive review. Energy Fuel. 35 (9), 7305–7318. https://doi.org/10.1021/acs.energyfuels.0c04082.
Wu, K., Chen, D., Zhang, W., et al., 2022. Movable fluid distribution characteristics and microscopic mechanism of tight reservoir in Yanchang Formation, Ordos Basin. Front. Earth Sci. 10, 840875. https://doi.org/10.3389/feart.2022.840875.
Xiong, J., Liu, X., Liang, L., 2015. Experimental study on the pore structure characteristics of the Upper Ordovician Wufeng Formation shale in the southwest portion of the Sichuan Basin, China. J. Nat. Gas Sci. Eng. 22, 530–539. https://doi.org/10.1016/j.jngse.2015.01.004.
Yang, W., Wang, Y., Xie, M., et al., 2023. Effect of lithofacies on differential movable fluid behaviors of saline lacustrine fine-grained mixed sedimentary sequences in the Jimusar sag, Junggar Basin, NW China: Forcing mechanisms and multi-scale models. Mar. Petrol. Geol. 150, 106150. https://doi.org/10.1016/j.marpetgeo.2023.106150.
Yang, Y., Qiu, L., Wan, M., et al., 2019. Depositional model for a salinized lacustrine basin: The Permian Lucaogou Formation, Jimsar sag, Junggar Basin, NW China. J. Asian Earth Sci. 178, 81–95. https://doi.org/10.1016/j.jseaes.2018.08.021.
Yang, Z., Hou H., L., Lin, S.H., et al., 2018. Geologic characteristics and exploration potential of tight oil and shale oil in Lucaogou Formation in Jimsar Sag. China Pet. Explor. 23 (4), 76–85. https://doi.org/10.3969/j.issn.1672–7703.2018.04.009 (in Chinese).
Yang, Z., Zou, C., Wu, S., et al., 2022. Characteristics, types, and prospects of geological sweet sections in giant continental shale oil provinces in China. J. Earth Sci. 33 (5), 1260–1277. https://doi.org/10.1007/s12583-022-1735-9.
Zha, X., Lai, F., Gao, X., et al., 2021. Characteristics and genetic mechanism of pore throat structure of shale oil reservoir in saline lake—A case study of shale oil of the Lucaogou Formation in Jimsar Sag, Junggar Basin. Energies 14 (24), 8450. https://doi.org/10.3390/en14248450.
Zhao, X., Pu, X., Jin, F., et al., 2019. Geological characteristics and key exploration technologies of continental shale oil sweet spots: A case study of Member 2 of Kongdian Formation in the Cangdong Sag in the Huanghua Depression, Bohai Bay Basin. Pet. Res. 4 (2), 97–112. https://doi.org/10.7623/syxb201908011 (in Chinese).
Zhang, W., Feng, Q., Wang, S., et al., 2019. Oil diffusion in shale nanopores: insight of molecular dynamics simulation. J. Mol. Liq. 290, 111183. https://doi.org/10.1016/j.molliq.2019.111183.
Zhang, C.J., Cao, J., Wang, Y.C., et al., 2022. Enrichment law of shale oil of Lucaogou Formation in Jimusar Sag, Junggar Basin. Acta Pet. Sin. 43 (9), 1253–1268. https://doi.org/10.7623/syxb202209005 (in Chinese).
Zhang, C., Jiang, F., Hu, T., et al., 2023a. Oil occurrence state and quantity in alkaline lacustrine shale using a high-frequency NMR technique. Mar. Petrol. Geol. 154, 106302. https://doi.org/10.1016/j.marpetgeo.2023.106302.
Zhang, X., Gao, Z., Maselli, V., 2023b. Pore structure and fractal characteristics of mixed siliciclastic-carbonate rocks from the Yingxi Area, Southwest Qaidam Basin, China. SPE Reservoir Eval. Eng. 26 (4), 1271–1291. https://doi.org/10.2118/215839-PA.
Zhang, Z.H., Zhang, T., Liu, H.Q., et al., 2024. Control and prediction of bedding-parallel fractures in fine-grained sedimentary rocks: A case from the Permian Lucaogou Formation in Jimusar Sag, Junggar Basin, Western China. Pet. Sci. 21 (6), 3815–3838. https://doi.org/10.1016/j.petsci.2024.09.003.
Zhi, D., Liu, X., Qin, Z., et al., 2021. Insights into the pore structure and fractal characteristics of Permian Lucaogou Formation shale from the Jimusar Sag, Junggar Basin. Arabian J. Geosci. 14, 1–15. https://doi.org/10.1007/s12517-021-06848-3.
Zou, C., Jin, X., Zhu, R., et al., 2015. Do shale pore throats have a threshold diameter for oil storage? Sci. Rep. 5 (1), 13619. https://doi.org/10.1038/srep13619.